Electronic Supplementary Material (ESI) for ChemComm.

Electronic Supplementary Information

Elucidating the Mechanism of the Structure-Dependent Enzymatic Activity of Fe-N/C Oxidase Mimic

Ying Wang,[a] Ziwei Zhang,[a] Guangri Jia,[a] Lirong Zheng,[c] Jingxiang Zhao,[b] and Xiaoqiang Cui[a*]*

Table of Contents

Experimental Procedures

Results and Discussion

Experimental Details

1. Chemicals and Materials

Multiwalled carbon nanotubes (MWCNTs) were purchased from Nanjing XFNANO Materials Tech Co., Ltd (China). Hydrogen peroxide (H_2O_2, 30%), nitric acid (HNO_3, 65.0~68.0%), zinc(II) nitrate hexahydrate ($Zn(NO_3)_2 \cdot 6H_2O$, 99.0%), 2-methylimidazole ($C_4H_6N_2$, 99.0%), nickel acetate tetrahydrate ($(CH_3COO)_2Ni \cdot 4H_2O$, 99.0%), cobaltous acetate tetrahydrate ($(CH_3COO)_2Co \cdot 4H_2O$, 99.0%), potassium thiocyanate (KSCN, AR), methanol (CH_3OH, >99.5%) acetic acid (HAc, AR), sodium acetate (NaAc, AR), sodium chloride (NaCl), *L*-cysteine, serine, lysine, asparagine, methionine, cysteine, ethanol (CH_3CH_2OH, AR), and dimethyl sulfoxide (DMSO) were all purchased from Sinopharm Chemical Reagent Co., China. Sulfuric acid (H_2SO_4, 95.0 ~ 98.0%), *t*-butyl alcohol (TBA, $C_4H_{10}O$), and hydrochloric acid (HCl, 35.0 ~ 38.0%) were obtained from Beijing Chemical Works, China. Iron(II) acetate ($(CH_3COO)_2Fe$, 99.0%) and 3,3',5,5'-tetramethylbenzidine (TMB) were obtained from Adamas-beta Chemical Co., Switzerland. Ferric oxide (Fe_2O_3, 99.9%), hemin ($C_{34}H_{32}ClN_4O_4Fe$, 95%), 2,2'-azinobis(3-ethylbenzthiazoline-6-sulfonate) (ABTS), *o*-phenylenediamine (OPD), catalase (≥ 200,000 unit/g), glutathione (GSH), *L*-ascorbic acid (AA), and *D*-(+)-glucose were obtained from Sigma-Aldrich (USA). *p*-Benzoquinone (*p*-BQ, $C_6H_4O_2$) was obtained from Shanghai MACKLIN Chemical Works, China. Nitrogen (N_2, high-purity, 99.999%) and argon (Ar, high-purity, 99.999%) were purchased from Xin'guang Gas Co., China. Human serum samples were obtained from a local hospital (China-Japan Union Hospital, Jilin University, Jilin, China). Deionized water from a Milli-Q system (18.2 MΩ·cm at 25 °C) was used throughout the experiments. All chemicals were used as received without further purification.

2. Characterization techniques

Scanning electron microscopy (SEM) images were obtained from an SU8010 field-emission scanning electron microscope (FESEM) at an accelerating voltage of 30 kV (Hitachi, Japan). The X-ray diffraction (XRD) patterns of the prepared samples were recorded

by powder XRD on a Bragg-Brentano diffractometer equipped with a Cu-Kα (λ = 0.15418 nm) emitting source (D8-tools, Germany). The scanning speed was set to $6°\cdot min^{-1}$. Transmission electron microscope (TEM) images were acquired by using a JEM-2100F transmission electron microscope (JEOL Co., Japan). The chemical state of the catalyst surface was analyzed by the ESCALAB-250 X-ray photoelectron spectroscopy (XPS) instrument (Thermo Fisher Scientific, USA) with a monochromatic Al-Kα (14, 866 eV) radiation source and a hemisphere detector using an energy resolution of 0.1 eV. Peak positions were corrected by the C 1s peak at 284.6 eV. Fe K-edge X-ray absorption spectra were obtained at Beijing Synchrotron Facility (BSRF) on beamline 1 W1B (XAFS station) at 2.2 GeV in fluorescence mode. The EXAFS raw

data were processed using the ATHENA module implemented in the IFEFFIT software packages according to the standard procedures of the background-subtracted, normalized and Fourier transformed. For the EXAFS fitting, theoretical scattering paths (Fe-O, Fe-Fe, Fe-C, and Fe-N) were calculated with FEFF6 using Artemis. Typical UV-vis spectra were obtained with a UV-2550 spectrometer (Shimadzu Co., Japan). Fluorescence (PL) spectra were obtained using an LS55 spectrometer (PerkinElmer Inc., USA). Inductively coupled plasma atomic emission spectroscopy (ICP-AES) data were collected with a JY2100 ICP-AES system (HORIBA, France). Optical photographs were acquired using an iPhone 7.

3. Computational Methods and Models

Our spin-polarized DFT computations were performed by using the DMol^3 code.[1] The electron interactions were described by the Perdew-Burke-Ernzerhof (PBE) exchange-correlation functional within the generalized gradient approximation (GGA).[2] The empirical correction in Grimme's scheme (i.e., DFT+D2) was utilized to treat (possible) van der Waals interactions.[3] The relativistic effects of transition metals were considered through the density functional semicore pseudopotential (DSPP),[4] in which a single effective potential and some degree of relativistic corrections replace the core electrons, while the double numerical plus polarization (DNP) basis set was used for other elements. Self-consistent field (SCF) computations were performed with a convergence criterion of 10^{-6} a.u. on the total energy and electronic computations. To ensure high-quality results, the real-space global

orbital cutoff radius was chosen as high as 5.2 Å in all computations.

The Fe-N_x/C-CNT (x = 0, 3,4, and 5) configurations observed in the experiment were modeled with a size of 12.30 Å × 12.30 Å × 20 Å (i.e., 5 × 5 supercells), in which all of the atoms were fully relaxed under geometric optimization. The adsorption energy (ΔE_{ads}) of the O_2 molecule on the catalysts was defined as $\Delta E_{ads} = E_{O_2\text{-catalyst}} - E_{O_2} - E_{catalyst}$, where $E_{O_2\text{-catalyst}}$, E_{O_2}, and $E_{catalyst}$ are the electronic energies of the adsorbed O_2 molecule on various catalysts, the free O_2 molecule, and the pristine catalyst, respectively. According to this equation, a more negative value suggests more stable adsorption. The energy of ($H^+ + e^-$) in solution at standard conditions is assumed as the energy of 1/2 H_2 for the theoretical calculation. The transition states were located by using the synchronous method with conjugated gradient refinements. This method involves linear synchronous transit (LST) maximization, followed by repeated conjugated gradient (CG) minimizations and then quadratic synchronous transit (QST) maximizations and repeated CG minimizations until a transition state is located.[5]

4. Synthesis of Catalysts

4.1 Preparation of the Metal (M = Fe, Co, Ni)-ZIF-8-CNT Precursors

Fe-ZIF-8-CNTs were produced according to our previous report with some modification.[6] In a typical synthesis, pre-treated MWCNTs (50 mg) were ultrasonically dispersed in methanol (60 mL) for 30 min to form a homogeneous solution in flask A; then, 2-methylimidazole (mIm) (0.748 g) was added to the solution and ultrasonicated for another 30 min. $(CH_3COO)_2Fe$ (9.90 mg) was dissolved in deionized water (10 mL) and then mixed with a methanol solution (50 mL) containing $Zn(NO_3)_2 \cdot 6H_2O$ (0.339 g) in flask B. Then, the contents of flask B were added into flask A and heated at 60 °C under intensive stirring for 24 h. The black products were separated via centrifugation and washed with water and ethanol three times respectively and dried at 60 °C in a vacuum oven overnight. The other metal-based (M = Co, Ni)-ZIF-8-CNTs were synthesized with a similar method using $(CH_3COO)_2Co \cdot 4H_2O$ (14.18 mg) or $(CH_3COO)_2Ni \cdot 4H_2O$ (14.16 mg) precursors. In addition, a series of different concentrations of iron in the precursors were named x Fe-ZIF-8-CNTs

(where x = 1 represented the addition of 3.3 mg of $(CH_3COO)_2Fe$ precursor).

4.2 Preparation of the Metal (M = Fe, Co, Ni)-N/C-CNT Catalysts

The obtained M-ZIF-8-CNTs precursors (50 mg) were heated to 900 °C (M = Co, Ni) or 1000 °C (M = Fe) at a rate of 5 °C min^{-1} in a tube furnace under an N_2 flow and maintained at this temperature for 1 hour. After gradually cooling to room temperature naturally, the black powder was soaked with an H_2SO_4 solution (1.0 M) for 5 hours at 60 °C to etch unstable inorganic metal phases. The leached sample was washed with deionized water several times and dried at 60 °C in a vacuum oven overnight.

5. Evaluation of the Oxidase-Like Activity of the Catalysts[7]

The oxidase-mimicking activity of the catalysts was investigated based on the oxidation of typical substrates (TMB, OPD, and ABTS), which resulted in the emergence of a characteristic absorption band at different wavelengths. A 5 mM TMB solution was diluted with 100 mM TMB (in dimethyl sulfoxide (DMSO)) stock solution. A homogeneous ink for the measurement was prepared by mixing the catalyst (1 mg) with deionized water (1.0 mL) followed by sonication for 60 min. In brief, the procedures were carried out as follows: TMB (5 mM, 50 μL) was added into an acetate buffer (pH = 4.0, 2400 μL). Subsequently, the Fe-N/C-CNT catalyst (1 $mg{\cdot}mL^{-1}$, 50 μL) was added to the analysis system. The mixture was incubated at room temperature for 10 min at 25 °C, and then UV–vis absorption spectroscopy was carried out.

6. Steady-State Kinetic Analysis[8]

Steady-state kinetic analysis of the reaction system was monitored by the corresponding time-dependent absorbance changes of TMB at 652 nm under the optimized conditions at certain time intervals. The values of the Michaelis-Menten constant were determined from the Lineweaver-Burk linear fitting plots derived from the Michaelis–Menten equation as follows: $1/v = (K_m/V_{max}) \times (1/[S]) + 1/V_{max}$, in which v stands for the initial reaction velocity, V_{max} represents the maximal reaction velocity, $[S]$ refers to the concentration of the substrate and K_m is the Michaelis–Menten constant.

7. The Colorimetric Assay for the Detection of GSH

GSH solutions of different concentrations were prepared by sequential dilution of the stock solution. The procedure for the detection of GSH was as follows: the TMB solution (15 mM, 25 μL) was added into an acetate buffer (pH = 5.0, 2425 μL). Subsequently, the Fe-N/C-CNT catalyst (1 $mg \cdot mL^{-1}$, 50 μL) was added to the analysis system. The mixture was incubated at room temperature for 10 min at 25 °C to ensure that the reaction was complete. A series of different concentrations of GSH were added into the above system and incubated for 5 min at 20 °C. Calibration curves between the change in absorbance intensity (ΔA, $\Delta A = A_0 - A$, where A_0 and A were the absorbance at 652 nm in the absence and presence of GSH, respectively) and various concentrations of GSH were plotted.

8. The Procedure for the Detection of GSH in Human Serum Samples[9]

The colorimetric analysis of GSH in human serum samples was approved by the ethics committee at Jilin University. Human serum samples were treated by centrifugation at 10000 rpm for 15 min. The supernatant was diluted 50 times with PBS buffer (pH = 7.4) to make the concentration of GSH suitable for the linear range. GSH detection was performed as described above in Section 7.

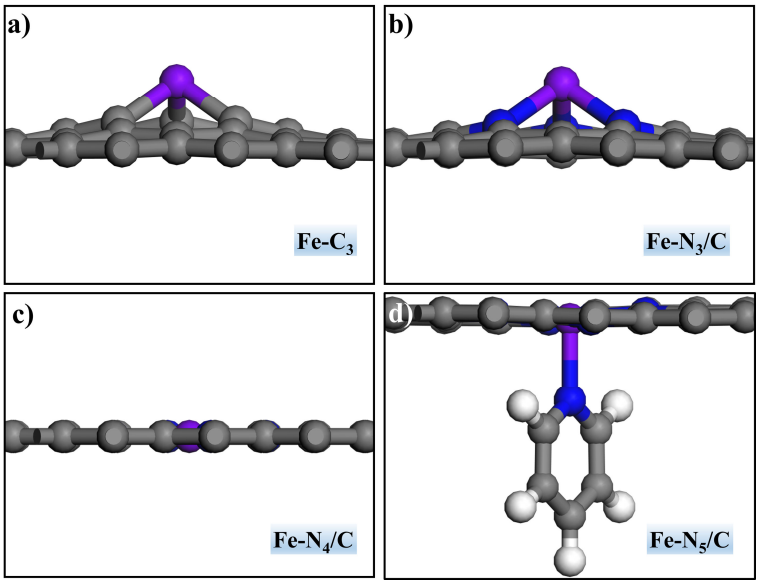

Figure S1. Side views of the (a) Fe-C_3, (b) Fe-N_3/C, (c) Fe-N_4/C, and (d) Fe-N_5/C structures.

The difference in the adsorption strength of these structures with O_2 molecule could be ascribed to two reasons: 1) Geometrical structure difference. The Fe-N_3/C or Fe-C_3 has a non-planar geometry in C_{3v} symmetry. These Fe atoms stand out of graphene plane, which are exposed in apical position above the graphene layer (Figure S1), thus indicating the superiority for O_2 adsorption than that of the planar geometry in the Fe-N_4 or Fe-N_5; 2) Magnetic moment difference. Spin moment is proved to be vital for the catalysts to the activation of small molecules.[10] The Fe atom in Fe-N_3 structure possesses the largest magnetic moment (about 3.16 μ_B) among all considered models, which is well consistent with its strongest interaction with O_2 molecule.

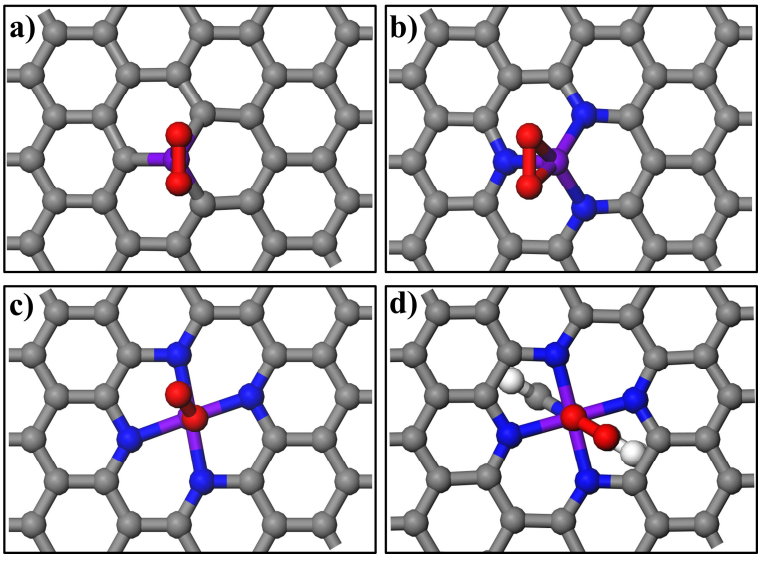

Figure S2. Top views of O_2 adsorption on the (a) Fe-C_3, (b) Fe-N_3/C, (c) Fe-N_4/C, and (d) Fe-N_5/C structures.

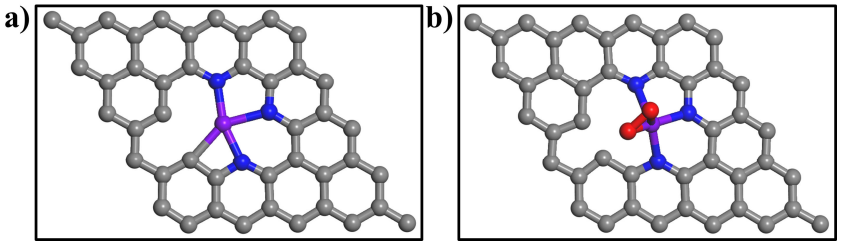

Figure S3. (a) The potential oxidase-like model with optimized structures of Fe-N_4 site with one nitrogen vacancy. (b) The top views of O_2 adsorption on the structure of Fe-N_4 site with one nitrogen vacancy.

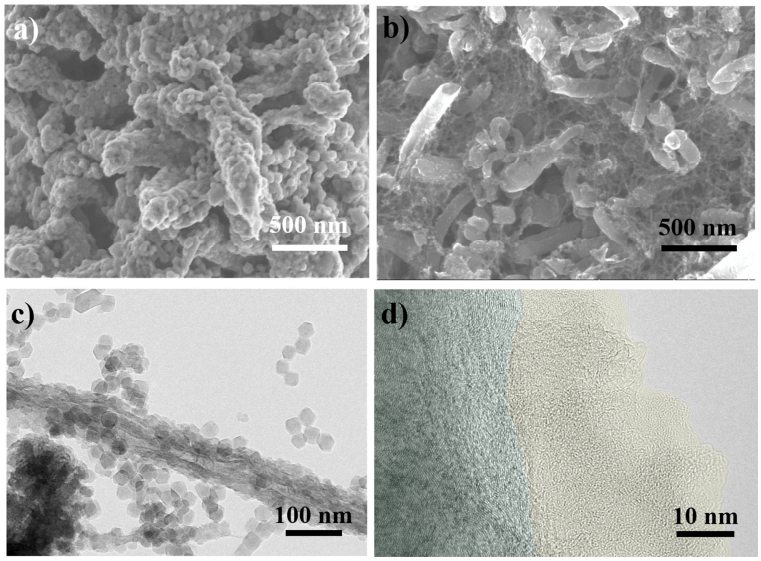

Figure S4. (a) SEM images of Fe-ZIF-8-CNT precursors. (b) SEM images of Fe-N/C-CNT catalysts. (c) TEM characterization of the morphology of the Fe-ZIF-8-CNT precursors. (d) TEM images of the Fe-N/C-CNT interfacial structure between amorphous carbon (green) and the graphitic carbon of the CNTs surface (yellow).

In the procedure of the synthesis of Fe-ZIF-8-CNT precursors, the MWCNTs were hydrophilic by a pre-treatment of the acid and H_2O_2 solution, which would be helpful for adsorbing the alkalescent ligand of 2-methylimidazole as the nucleation sites on the surfaces of CNTs for the growth of Fe-ZIF-8. As given in the Figure S4a and Figure S4c, the surface of CNTs is uniformly coated by Fe-ZIF-8 nanocrystals, which are not the well-defined rhombic dodecahedron shapes. After thermal treatment at 1000 °C, Zn species in ZIFs are easily evaporated (> 907 °C) and the hydrocarbon networks in ZIF crystals are completely carbonized to form the amorphous carbon (Figure S4b and Figure S4d), which makes the already irregular skeleton collapsed. But the introduction of CNTs plays a great role in avoiding the further agglomeration of the derived amorphous carbon and induces the evolution into sheet-like morphology on the surface of CNTs.

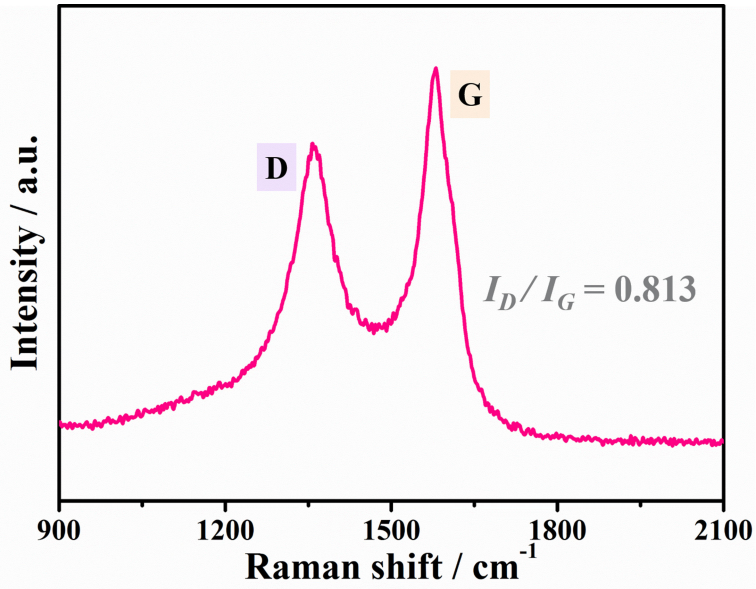

Figure S5. Raman spectrum of Fe-N/C-CNT catalysts.

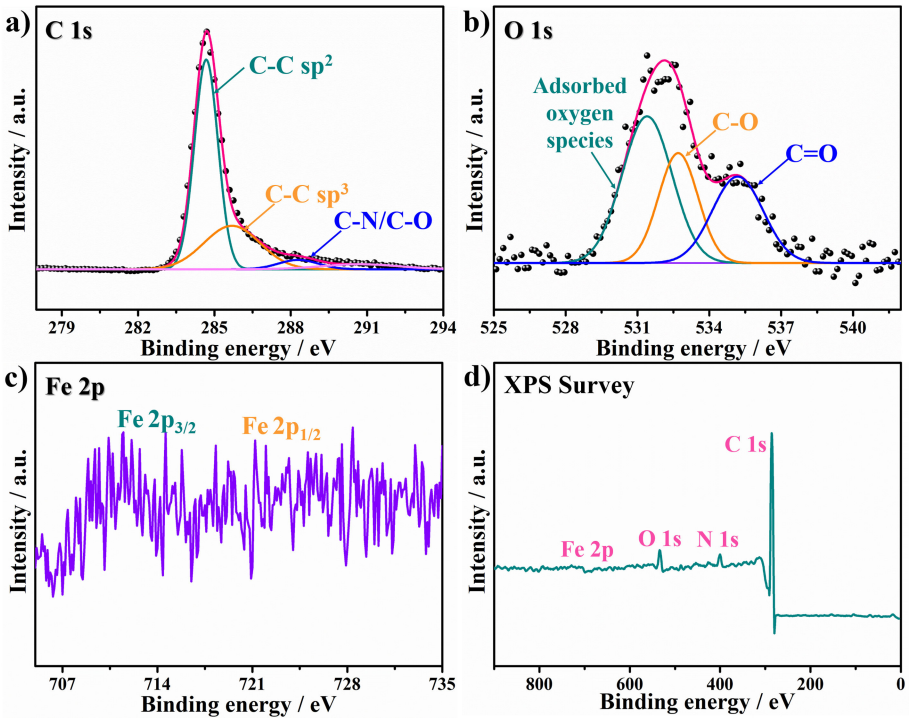

Figure S6. High-resolution XPS spectra of (a) C 1s, (b) O 1s, and (c) Fe 2p and (d) XPS survey scan for Fe-N/C-CNT catalysts.

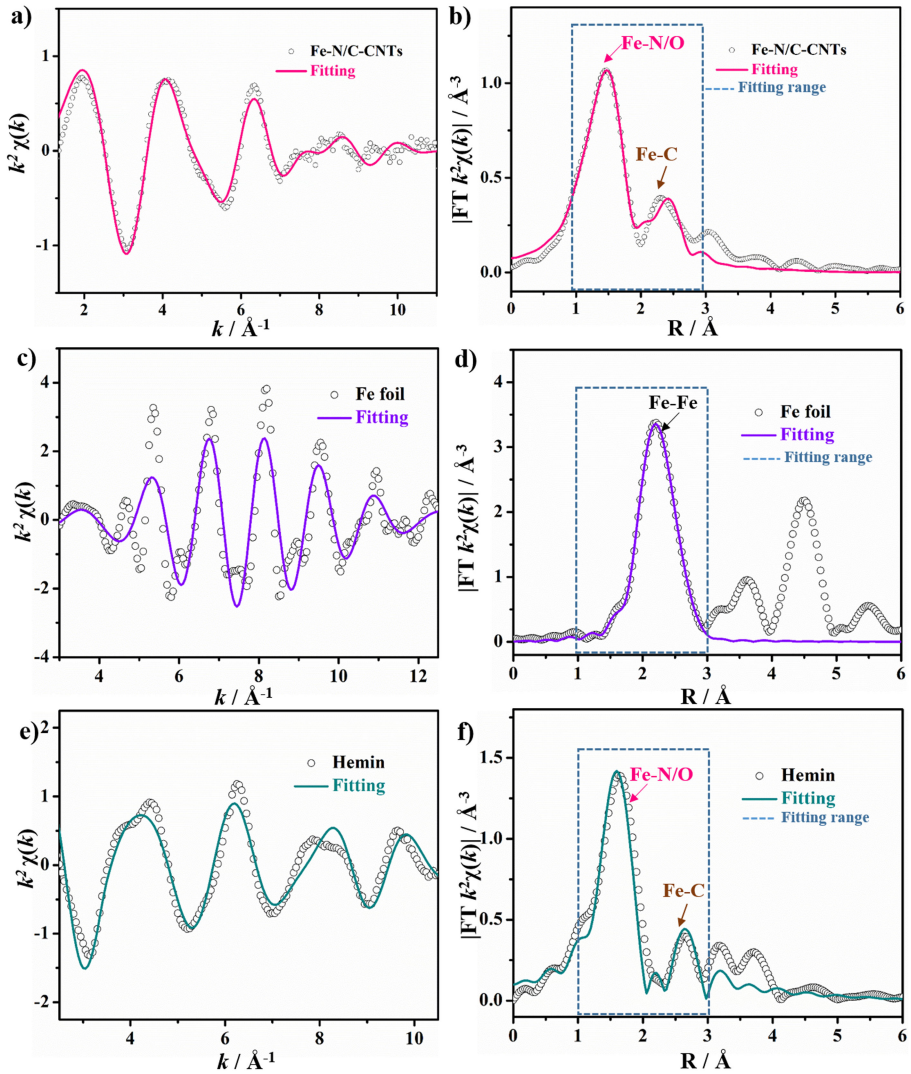

Figure S7. The k^2-weighted EXAFS fitting curves in k-space and their Fourier transforms in the R domain of Fe-N/C-CNTs (a-b), Fe foil (c-d), and hemin (e-f).

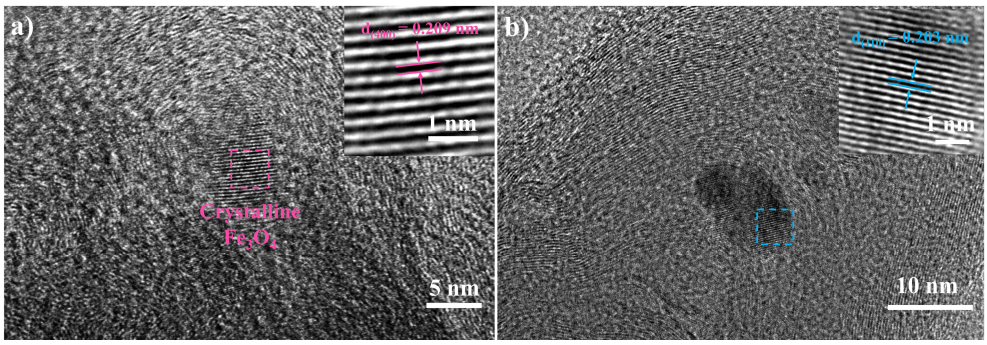

Figure S8. HRTEM images of the trace metallic iron (oxide) species existed in the Fe-N/C-CNTs catalysts.

As observed in HRTEM image (Figure S8), small iron (oxide) and Fe_3C nanocrystals with the crystalline lattice of 0.209 nm and 0.203 nm are encased by the graphitic layers, which could be derived from partial Fe-N bonds in the procedure of high-temperature pyrolysis and are hardly removed by the acid-washing with the protection of the graphitic layers.

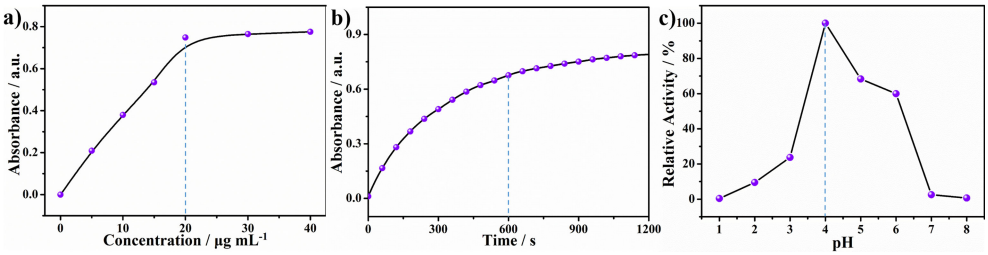

Figure S9. Effects of different (a) concentrations of catalysts, (b) incubation time, and (c) pH on the oxidase-like catalytic activity of Fe-N/C-CNTs.

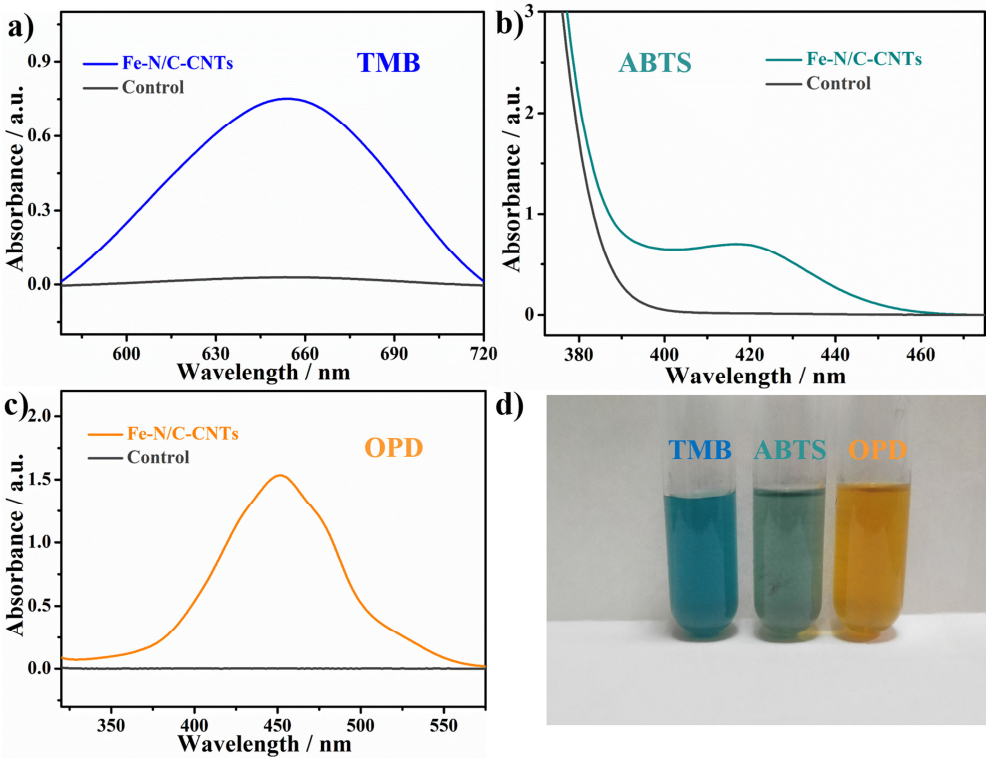

Figure S10. UV-vis spectra of reaction products during the oxidation of (a) TMB, (b) ABTS, and (c) OPD catalyzed by Fe-N/C-CNT catalysts. (d) The corresponding color changes during the reaction.

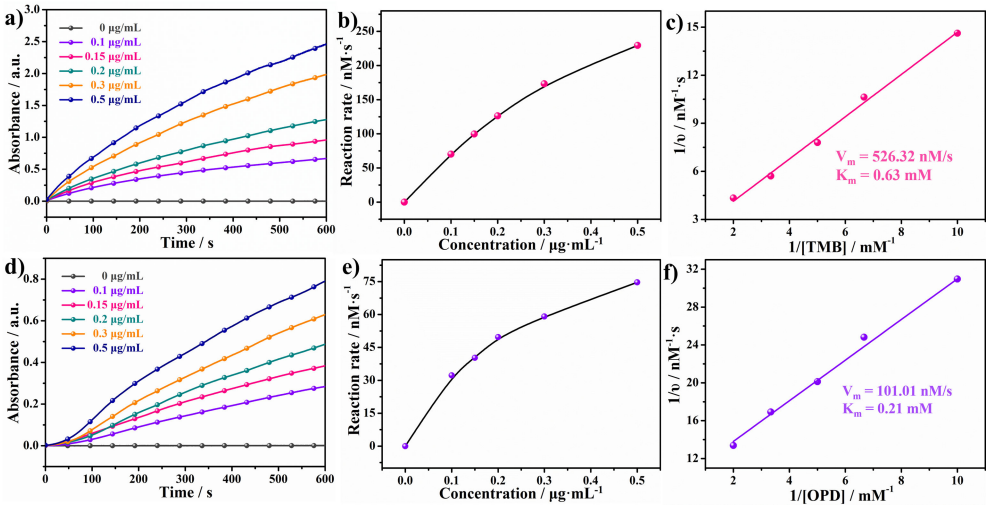

Figure S11. Kinetic analysis and the corresponding double-reciprocal plots for calculation of enzyme kinetic parameters by the Michaelis-Menten equation of the oxidase-like reaction with TMB (a-c) or OPD (d-f) for the Fe-N/C-CNTs system.

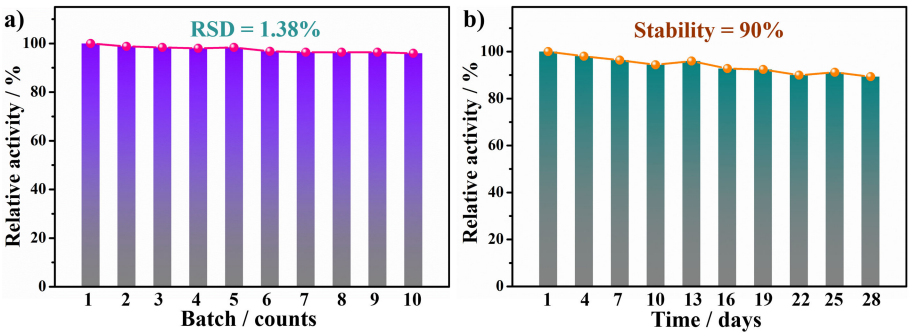

Figure S12. The relative activity of the Fe-N/C-CNT system during different (a) batches and (b) days. The activity of freshly prepared Fe-N/C-CNT catalysts is set as 100%.

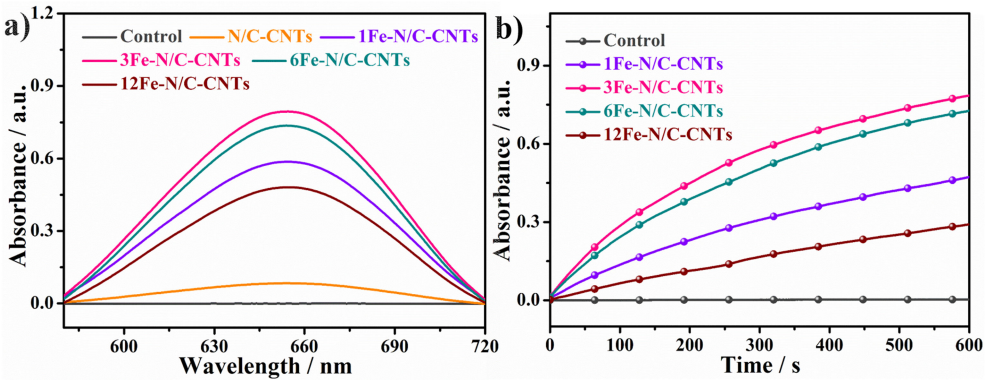

Figure S13. (a) UV-vis spectra of reaction products during the oxidation of TMB catalyzed by the Fe-N/C-CNT catalysts with different iron contents. (b) The corresponding time-dependent absorbance changes of TMB at 652 nm.

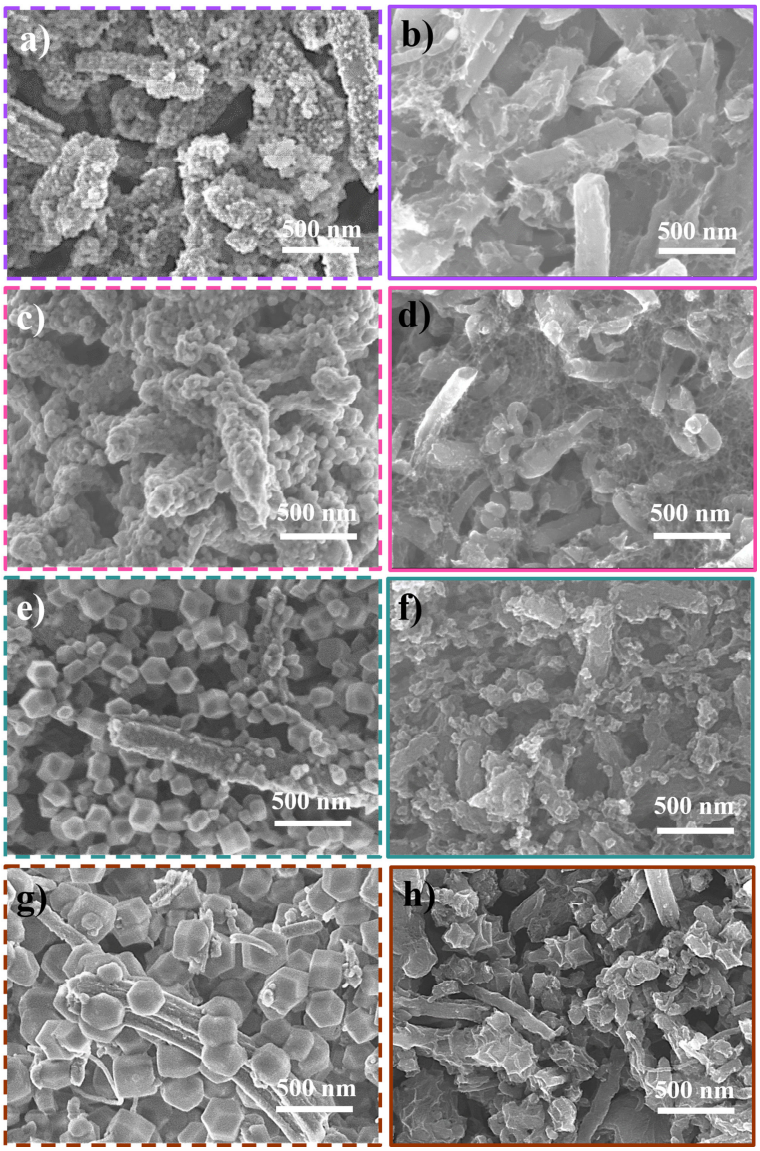

Figure S14. SEM images of catalysts with different amounts of Fe without and with annealing: a-b) 1Fe, c-d) 3Fe, e-f) 6Fe, and g-h) 12Fe.

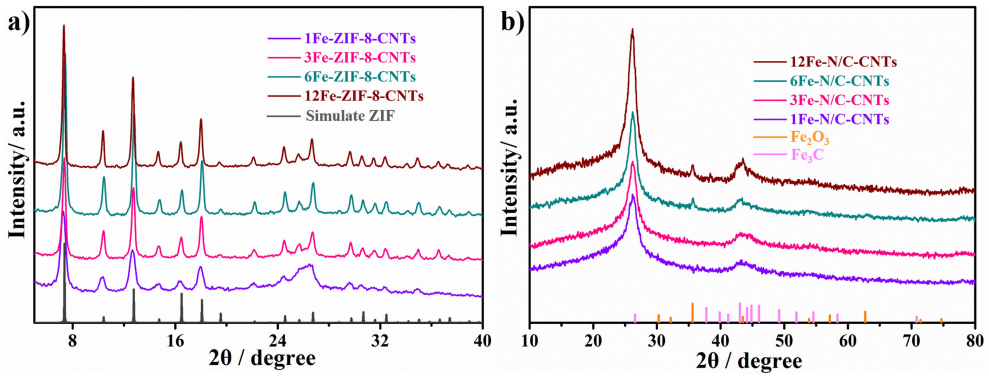

Figure S15. XRD patterns for catalysts with different amounts of Fe (a) without and (b) with annealing. (Fe_2O_3 PDF# 24-0081; Fe_3C PDF# 03-0989)

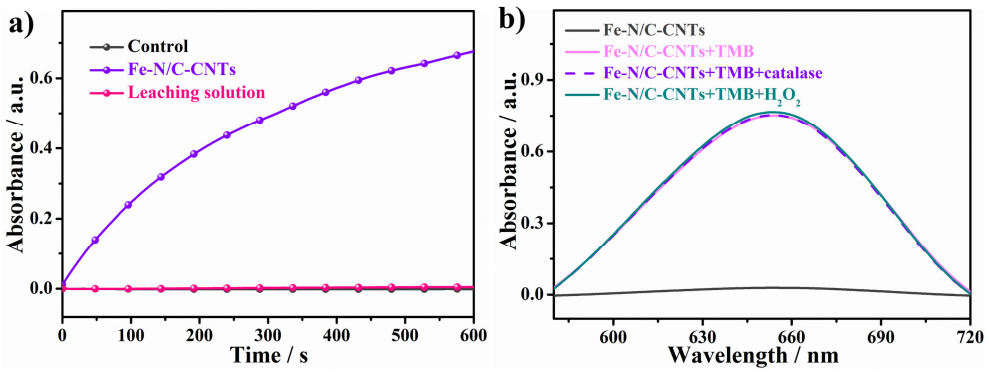

Figure S16. (a) Demonstration that the oxidase-like activity of Fe-N/C-CNTs did not result from iron ion leaching. (b) UV-vis spectrum of the reaction products during the oxidation of TMB catalyzed by Fe-N/C-CNT system in the absence and presence of H_2O_2 or catalase.

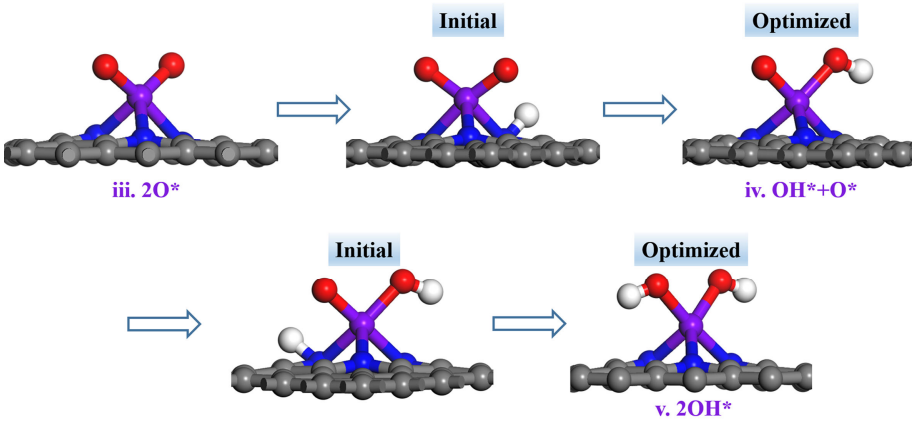

Figure. S17 The initial and optimized structures of H adsorption on $2O^*$, O^*-OH^*, and $2OH^*$ species, respectively.

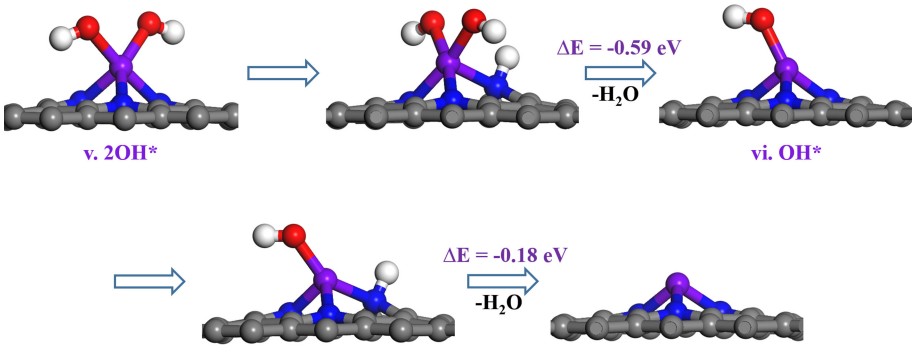

Figure. S18 The optimized structures of the procedure for the release of H_2O.

For the obtained structures from (iii) to (v), as well as the release of H_2O, we considered a two-step adsorption, i.e., (1) the catalyst firstly loots H^+ from solvent to its N atoms due to the electrostatic attraction between the positively charged H^+ and negatively charged N atom to form the adsorbed H species (H*); (2) the H* species is transferred from N atom to the O* atom to form O*-OH*, OH*-OH*, OH*-H_2O (*aq.*), and $2H_2O$ (*aq.*). Thus, on the basis of the above analysis, the computations for the H adsorption on N atom, in which the initial and optimized structures, as well as their energy difference are both presented. As shown in **Figure S17**, although we considered H adsorption on the N atom nearby Fe site, it will be spontaneously optimized to O* atom to form O*-OH^* and $2OH^*$. Once the $2OH^*$ species is formed, it will loot one H^+ from solvent to form H^* species (**Figure S18**). Subsequently, the H^* species approaches one OH^* group to release one H_2O with the exothermicity of 0.59 eV. Similar case can be observed for the release of the second H_2O with a small exothermicity of 0.18 eV.

As follows, the whole reaction process is illustrated by the following equation: [11]

O_2 (g) → O_2*

O_2* → 2O*

2O* + (H^+ + e^-) → O* + OH*

O* + OH* + (H^+ + e^-) → 2OH*

2OH* + (H^+ + e^-) → OH* + H_2O (*aq.*)

OH* + H_2O (*aq.*) + (H^+ + e^-) → $2H_2O$ (*aq.*)

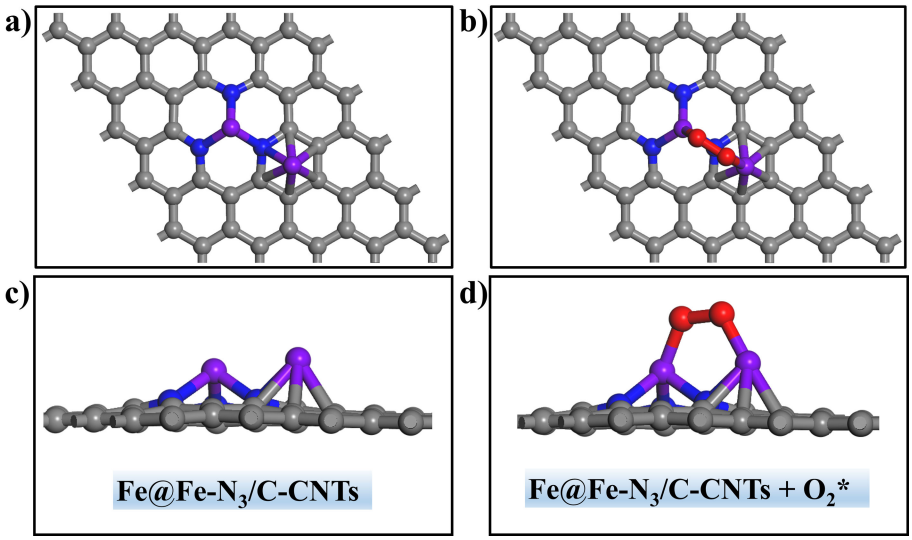

Figure S19. The (a-b) top and (c-d) side views of O_2 adsorption on the structure of Fe@Fe-N_3/C-CNTs structure.

Notably, this catalyst exhibits too strong adsorption strength toward O_2 ($E_{ads.}$ = –4.11 eV) to release the product according to the Sabatier principle that an ideal catalyst should moderately (not too strongly or too weakly) interact with the target molecule.[12]

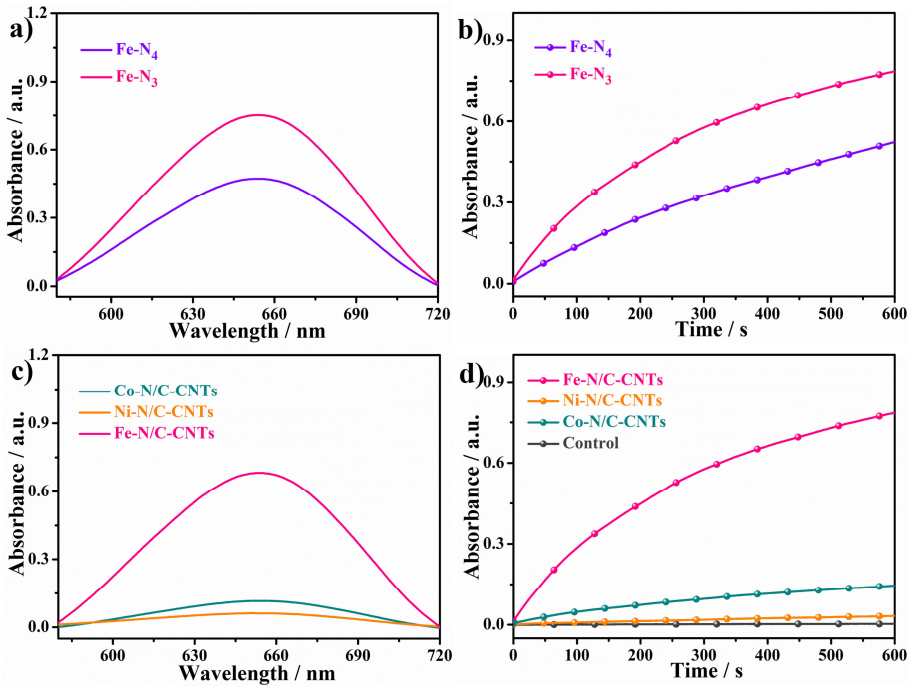

Figure S20. UV-Vis spectrum of reaction products during the oxidation of TMB and the corresponding time-dependent absorbance changes of TMB at 652 nm in the presence of (a-b) different Fe-N coordination in catalysts and (c-d) different metal-N/C-CNT catalysts.

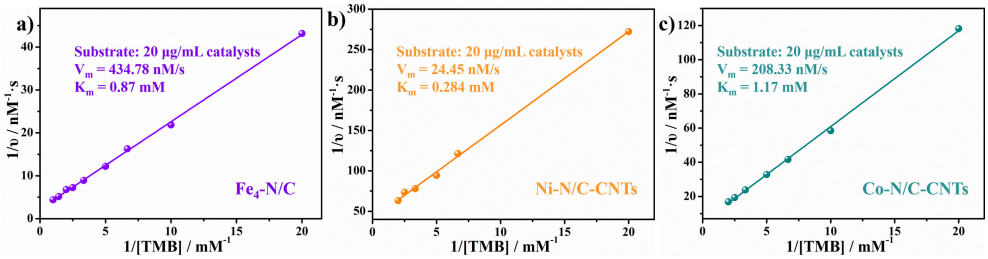

Figure S21. The double-reciprocal plots for calculation of the enzyme kinetic parameters of the oxidase-like reaction with TMB by the Michaelis-Menten equation for the (a) Fe-N_4, (b) Ni-N/C-CNT, and (c) Co-N/C-CNT systems.

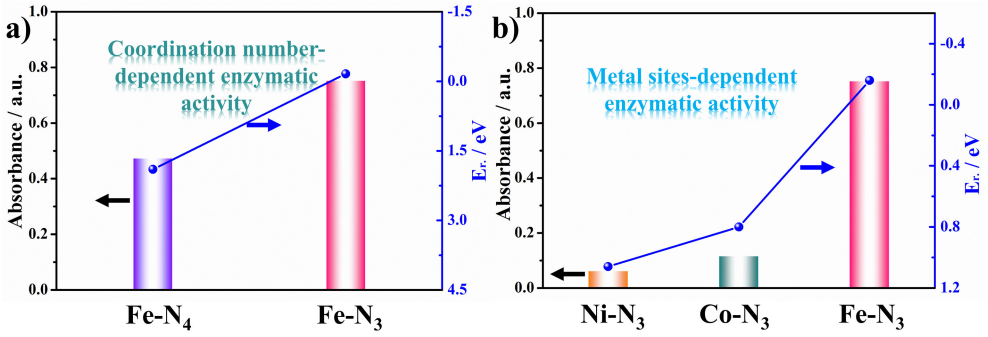

Figure S22. (a) The correlation between the coordination number-dependent enzymatic activity and theoretically thermodynamic energies. (b) The correlation between the metal sites-dependent enzymatic activity and theoretically thermodynamic energies.

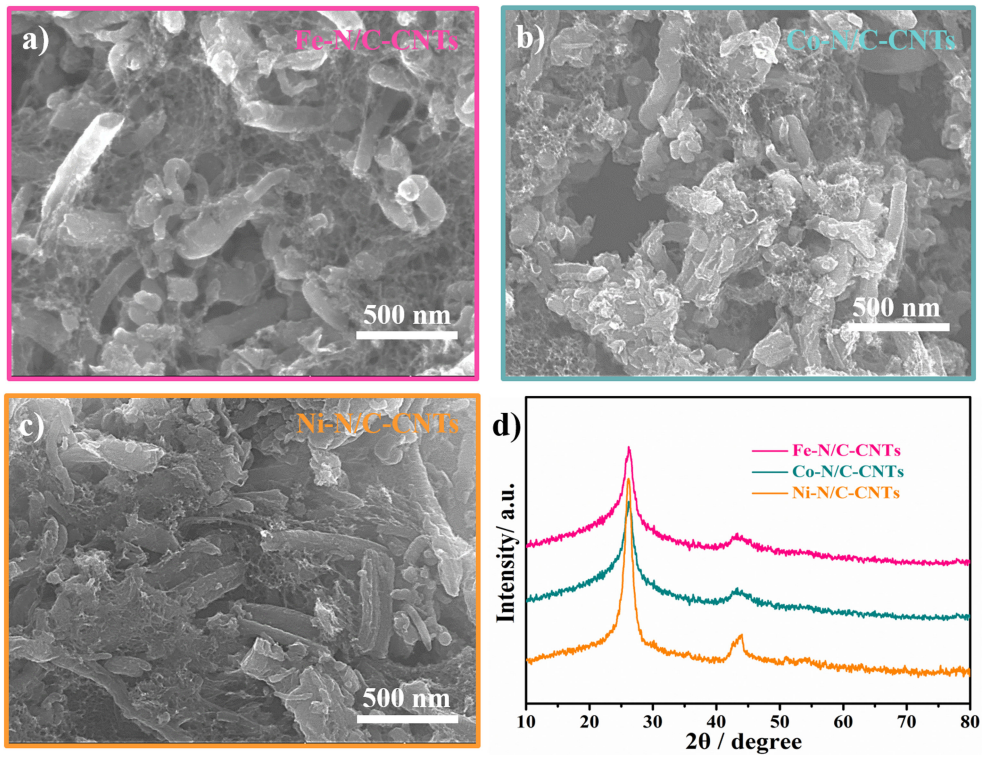

Figure S23. SEM images for catalysts with different metal-N/C-CNTs: a) Fe, b) Co, and c) Ni. (d) The XRD results for catalysts composed of different metals.

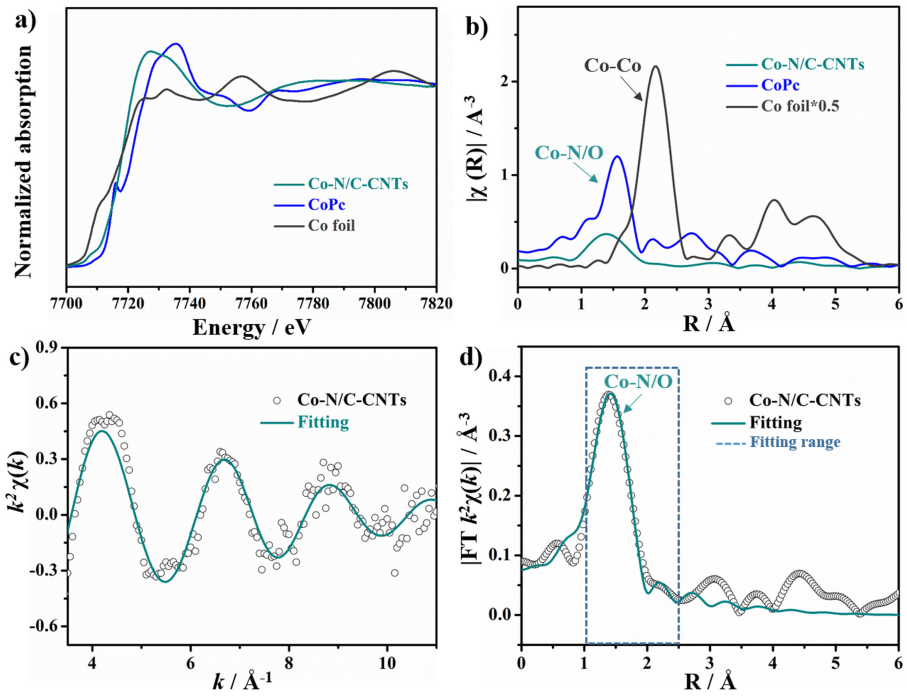

Figure S24. (a) Co K-edge XANES spectra. (b) k^2-weighted FT-EXAFS spectra. The k^2-weighted EXAFS fitting curves of Co-N/C-CNTs (c) in *k*-space and (d) the Fourier transforms in the R domain.

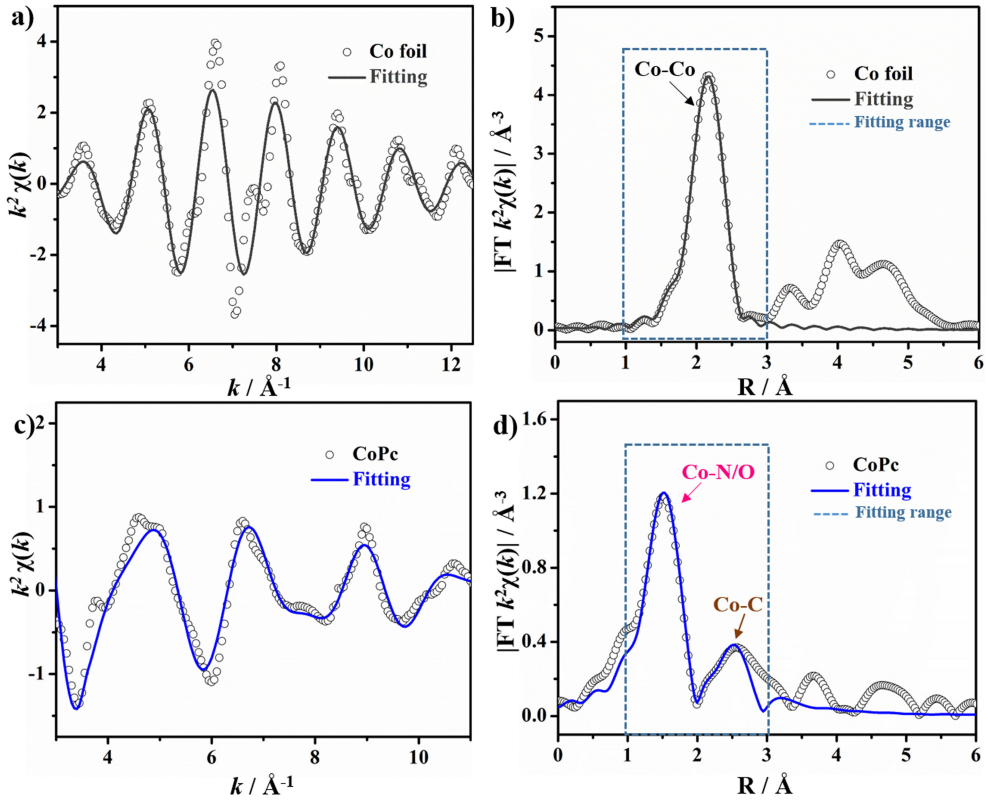

Figure S25. The k^2-weighted EXAFS fitting curves in *k*-space and their Fourier transforms in the R domain of Co foil (a-b) and CoPc (c-d).

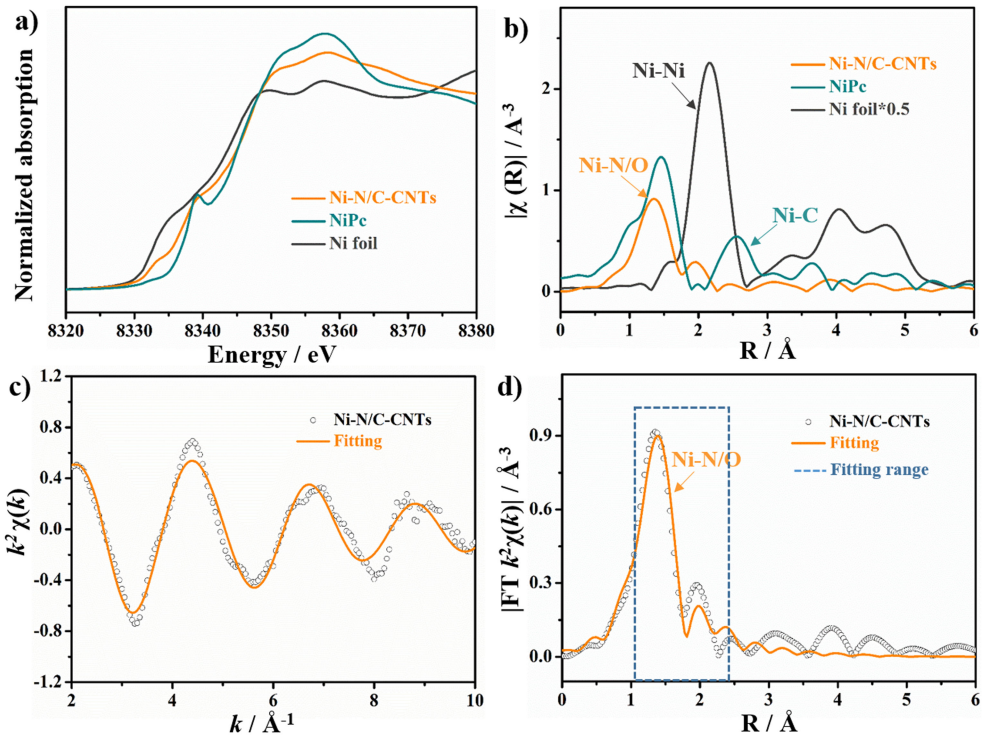

Figure S26. (a) Ni K-edge XANES spectra. (b) k^2-weighted FT-EXAFS spectra. The k^2-weighted EXAFS fitting curves of Ni-N/C-CNTs (c) in *k*-space and (d) the Fourier transforms in the R domain.

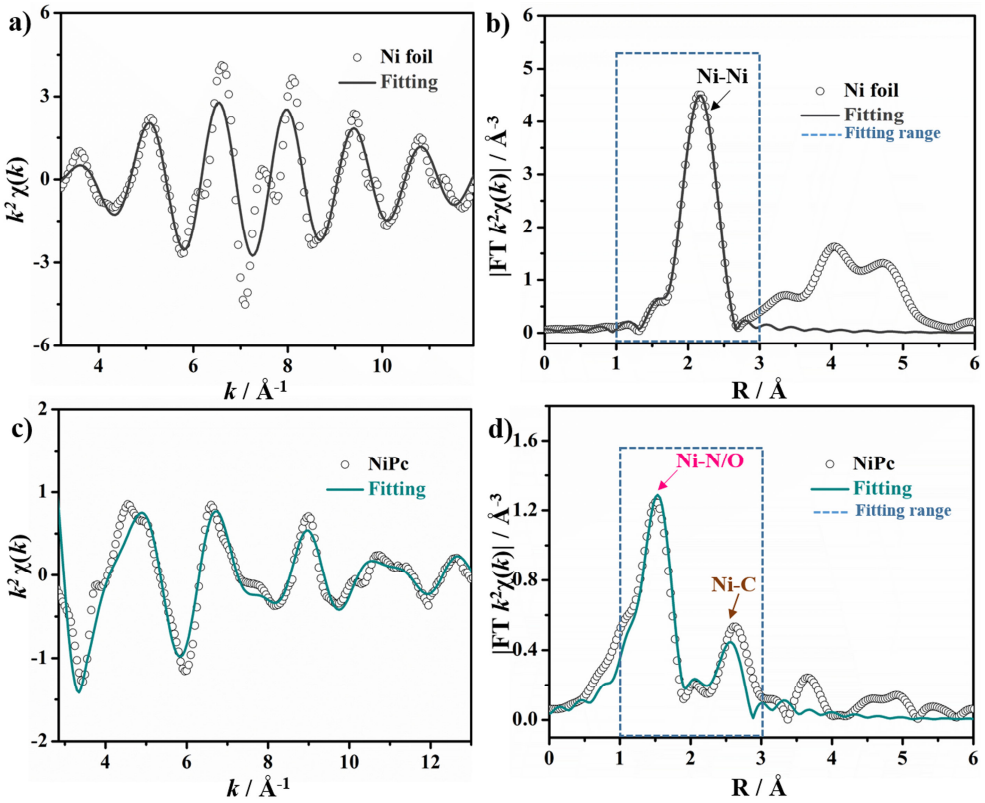

Figure S27. The k^2-weighted EXAFS fitting curves in *k*-space and their Fourier transforms in the R domain of Ni foil (a-b) and NiPc (c-d).

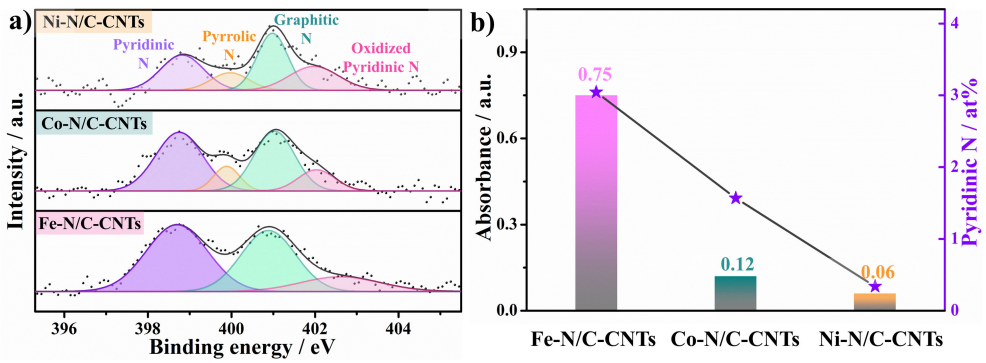

Figure S28. (a) The high-resolution XPS spectra of N 1s with different metal-N/C-CNTs. (b) The relationship between the absorbance changes of TMB at 652 nm and the pyridinic-N contents of the M-N/C-CNT catalysts (M = Fe, Co, Ni).

Although the preparation of metal (M = Fe, Co, Ni)-N/C-CNTs all utilizes ZIF-8 as self-sacrificed precursor/template, the nitrogen species in the final Fe, Co, and Ni-N/C-CNTs are derived from the corresponding skeleton of organic-ligand.

Ni-N/C-CNTs have the lowest nitrogen content is attributed to its weakest coordination ability to the organic-ligand than the Fe, Co-based materials. The similar local coordination environment make Co^{2+} and Fe^{2+} substitution for Zn^{2+} in ZIF-8 more favorable than Ni^{2+}, which can possess more nitrogen content in the final pyrolysis products than Ni-based products.

The different nitrogen content between Fe- and Co-based materials is caused by the high-heat treatment. Cobalt is a widely used catalyst for CNT growth,[13] which is more likely to be reduced metallic Co nanoparticles and leads to the loss of nitrogen contents.

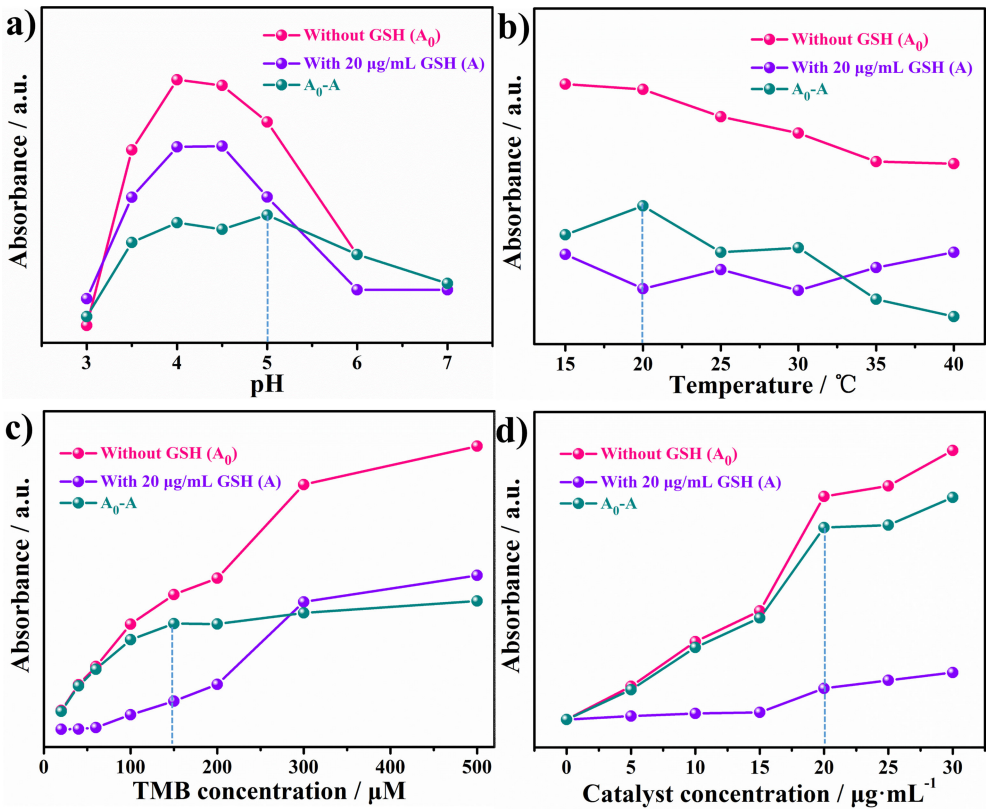

Figure S29. Effects of different (a) pH, (b) temperatures, (c) TMB concentrations, and (d) concentrations of catalysts on the detection of GSH using Fe-N/C-CNTs.

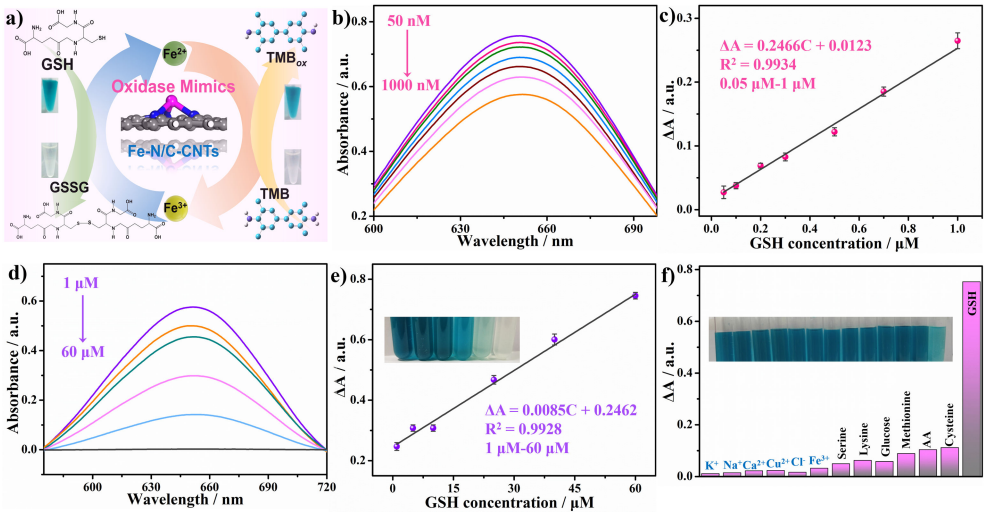

Figure S30. (a) Schematic illustration of the Fe-N/C-CNT catalysts as oxidase-like mimics for GSH sensing. UV–vis absorbance spectra of TMB incubated with Fe-N/C-CNT catalysts in the presence of various concentrations of GSH ranging from (b) 50 to 1000 nM and (d) 1 to 60 μM. (c and e) The corresponding calibration plots between the change in absorbance intensity (ΔA) and GSH concentration. (f) Selectivity for GSH over different potential interfering agents.

The intrinsic oxidase-like activity of as-prepared Fe-N/C-CNTs is applied as a feasible colorimetric platform for glutathione (GSH) detection based on the selective inhibition of TMB oxidation. Under the optimized reaction conditions (Figure S29), the calibration curves show linear relationships in the ranges from 50 nM to 1 μM and from 1 μM to 60 μM (Figure S30a-S30e), which are much wider than those of the other sensing probes listed in Table S4. This proposed system also shows superior selectivity to different interferential substances (Figure S30f). The practical feasibility and accuracy of the developed biosensing assay are also evaluated by the analysis of the GSH concentration in human serum samples and corresponding standard addition studies. The satisfactory recoveries from 95.9% to 103.8% indicate the great potential reliability of Fe-N/C-CNTs in biological systems for the detection of GSH (Table S5).

Table S1. The K-edge EXAFS curves fitting parameters.

Sample	Path	Coordination Number	Bond length R [Å]	Bond disorder σ^2 [$\times10^{-3}$Å^2]	$\triangle E_0$ [eV]	R, %
Fe foil	Fe-Fe	8*	2.46±0.01	4.2±1.2	4.9±1.1	0.006
	Fe-Fe	6*	2.85±0.01			
Co foil	Co-Co	12*	2.49±0.01	6.3±0.2	0.7±0.1	0.001
Ni foil	Ni-Ni	12*	2.48±0.01	6.1±0.3	6.3±0.4	0.002
Hemin	Fe-N	4.5±1.2	2.06±0.02	6.6±3.4	7.4±2.8	0.016
	Fe-C	4.8±2.0	3.09±0.04			
CoPc	Co-N	4.1±0.9	1.92±0.01	3.0±1.7	10.2±2.7	0.017
	Co-C	7.6±2.0	2.94±0.02			
NiPc	Ni-N	4.6±0.8	1.91±0.01	3.6±1.5	8.4±2.8	0.013
	Ni-C	7.4±1.9	2.92±0.02			
Fe-N/C-CNTs	Fe-N	2.9±0.4	2.01±0.01	9.7±1.9	−1.1±0.8	0.5
	Fe-Fe	2.7±1.0	3.00±0.02			
Co-N/C-CNTs	Co-N	3.2±1.1	1.87±0.02	6.1±2.7	7.8±3.7	0.014
Ni-N/C-CNTs	Ni-N	2.7±0.5	1.89±0.02	6.3±3.6	−6.3±1.9	0.014

Table S2. The comparation of apparent Michaelis-Menten constant (K_m), maximum reaction rate (V_{max}), and catalytic constant ($k_{cat.}$) of different catalysts as oxidase mimetic.

Catalyst	Substance	K_m [mM]	V_{max} [M·s^{-1}]	$k_{cat.}$ [s^{-1}]	Reference
Fe-N/C-CNTs	TMB	0.62	5.26×10^{-7}	1.48	*This work*
	OPD	0.21	1.01×10^{-7}	0.28	
Ni-N/C-CNTs	TMB	0.284	2.45×10^{-8}	0.056	
Co-N/C-CNTs	TMB	1.17	2.08×10^{-7}	0.307	
Fe SAEs	TMB	0.13	2.25×10^{-8}	-	*Chem. Commun.*, **2019**, 55, 2285-2288
	OPD	0.066	1.52×10^{-8}	-	
N-PCNSs	TMB	0.084	4.2×10^{-9}	-	*Nat. Commun.*, **2018**, 9, 1440
Fe_3C/N−C	TMB	0.225	3.25×10^{-7}	-	*ACS Sustainable Chem. Eng.* **2018**, 6, 16766-16776
MOF(Co/2Fe)	TMB	0.199	3.9×10^{-9}	-	*Microchim. Acta*, **2017**, 184, 4629
Pt nanoclusters	TMB	0.63	27×10^{-7}	-	*Nanoscale*, **2014**, 6, 9618
Au@Pt	TMB	0.031	2.5×10^{-8}	-	*Biomaterials,* **2011**, 32, 1139
Ag-$CoFe_2O_4$/rGO	TMB	2.09	-	-	*Chem. Eng. J.* **2018**, 350, 120
EMSN-AuNPs	TMB	0.3	1.19×10^{-7}	-	*Adv. Mater.* **2015**, 27, 1097

Table S3. Summary of elemental quantification determined by using XPS as a function of different catalysts.

Catalyst	C	N	O	Fe	Relative concentrations of different N species (area%)			
	at.%				Pyridinic N	Pyrrolic N	Graphitic N	Oxidized Py. N
Fe-N/C-CNTs	89.44	6.5	3.05	1.01	46.82	-	42.86	10.33
Co-N/C-CNTs	90.4	4.39	4.08	0.93	35.7	15.01	36.43	12.86
Ni-N/C-CNTs	93.26	1.28	4.69	0.77	26.38	13.11	42.66	17.85

Table S4. The analytical performance of glutathione by different metal oxides and metal ions based sensing probe.

Sensing platform	Method	Linear range	*Reference*
Fe-N/C-CNTs	Colorimetry (TMB)	50 nM-1 μM 1 μM-60 μM	This work
V_2O_5 nanosheets	Colorimetry (TMB)	0.01 μM-0.5 μM	*Sensor. Actuat. B.* ***2018,*** 273, 1179
MnO_2 nanosheets	Colorimetry (TMB)	1 μM-25 μM	*Biosens. Bioelectron.* ***2017***, 90, 69
Co,N-HPC	Colorimetry (TMB)	0.05 μM-30 μM	*Sensor. Actuat. B.* ***2018,*** 264, 312
MnO_2	Colorimetry (TMB)	0.3 μM-15 μM	*Sensor. Actuat. B.* ***2018,*** 258, 80
CeO_2 NPs	Colorimetry (TMB)	0.0 μM-40 μM	*Chem. Commun.,* **2015**, 51, 4635
carbon dots–MnO_2	Fluorimetry	1 μM-10 μM	*Biosens. Bioelectron.* **2015**, 72, 31
$Fe(CN)_6^{3-/4-}$/CDs	Electro-chemistry	0.05 μM-30μM	*Anal. Chem.* **2015**, 87, 11150
Lanthanide-MnO_2	Photoluminescence	-	*J. Am. Chem. Soc.* **2011**, 133, 20168
Arg-AuNPs	Fluorimetry	0.12 μM-1 μM	*Small* **2015**, 11, 5510

Table S5. Results for the determination of GSH concentration in human serum samples.

Serum sample	GSH Spiked [μM]	GSH Measured [μM]	Recovery [%]	RSD (n = 3)
Human Serum	0	0.277 ± 0.01	0	3.76
	0.15	0.421 ± 0.01	95.9	2.80
	0.30	0.576 ± 0.01	99.5	2.04
	0.50	0.796 ± 0.01	103.8	1.69

References

1. B. Delley, *J. Chem. Phys.* **2000**, *113*, 7756-7764.

2. J. P. Perdew, K. Burke, M. Ernzerhof, *Phys. Rev. Lett.* **1996**, *77*, 3865-3868.

3. S. Grimme, *J. Comput. Chem.* **2006**, *27*, 1787-1799.

4. B. Delley, *Phys. Rev. B* **2002**, *66*, 155125.

5. N. Govind, M. Petersen, G. Fitzgerald, D. King-Smith, J. Andzelm, *Comp. Mater. Sci.* **2003**, *28*, 250-258.

6. Y. Wang, X. Q. Cui, J. X. Zhao, G. R. Jia, L. Gu, Q. H. Zhang, L. K. Meng, Z. Shi, L. R. Zheng, C. Y. Wang, Z. W. Zhang, W. T. Zheng, *ACS Catal.* **2019**, *9*, 336-344.

7. B. Jiang, D. M. Duan, L. Z. Gao, M. J. Zhou, K. L. Fan, Y. Tang, J. Q. Xi, Y. H. Bi, Z. Tong, G. F. Gao, N. Xie, A. F. Tang, G. H. Nie, M. M. Liang, X. Y. Yan, *Nat. Protoc.* **2018**, *13*, 1506-1520.

8. L. Z. Gao, J. Zhuang, L. Nie, J. B. Zhang, Y. Zhang, N. Gu, T. H. Wang, J. Feng, D. L. Yang, S. Perrett, X. Y. Yan, *Nat. Nanotechnol.* **2007**, *2*, 577.

9. J. Liu, L. J. Meng, Z. F. Fei, P. J. Dyson, X. N. Jing, X. Liu, *Biosens. Bioelectron.* **2017**, *90*, 69-74.

10. J. X. Zhao, Z. F. Chen, *J. Am. Chem. Soc.* **2017**, *139*, 12480-12487.

11. M. S. Kim, S. Cho, S. H. Joo, J. Lee, S. K. Kwak, M. I. Kim, J. Lee, *ACS Nano* **2019**, DOI: 10.1021/acsnano.8b09519.

12. J. Kari, J. P. Olsen, K. Jensen, S. F. Badino, K. B. R. M. Krogh, K. Borch, P. Westh, *ACS Catal.* **2018**, *8*, 11966-11972; P. Sabatier, *Ber. Dtsch. Chem. Ges.* **1911**, *44*, 1984-2001.

13. J. Wang, D. F. Gao, G. X. Wang, S. Miao, H. H. Wu, J. Y. Li, X. H. Bao, *J. Mater. Chem. A* **2014**, *2*, 20067-20074.